Structure and magnetism of Fe-doped SnO_2 nanoparticles

R. Adhikari and A. K. Das*
Department of Physics & Meteorology, Indian Institute of Technology, Kharagpur 721302, India

D. Karmakar and T. V. Chandrasekhar Rao
Technical Physics & Prototype Engineering Division, Bhabha Atomic Research Center, Mumbai 400085, India

J. Ghatak
Institute of Physics, Sachivalaya Marg, Bhubaneswar 751005, India

(Received 28 February 2008; published 3 July 2008)

SnO_2 nanoparticles doped with Fe of different concentrations were synthesized by a chemical coprecipitation method. After calcination at 600 °C, the samples were characterized using x-ray diffraction (XRD), transmission electron microscope (TEM), and superconducting quantum interference device magnetometer. XRD shows that the solubility of Fe in SnO_2 ($Sn_{1-x}Fe_xO_2$: primary phase where Fe substitutes Sn in SnO_2 matrix) is less than 7.5% ($x<0.075$) and Fe_2O_3 (hematite) or $(Fe_{1-y}Sn_y)_2O_3$ (where Sn substitutes Fe in Fe_2O_3 matrix) is evolved as a secondary phase for $x \geq 0.075$ along with $Sn_{1-x}Fe_xO_2$ (primary phase). TEM shows that the particles are crystalline and of size in the nanometric regime (10 ± 3 nm). The $M(T)$ and $M(H)$ studies indicated an antiferromagnetic (AFM) interaction in 3% and 5% (atomic weight) Fe-doped SnO_2 nanoparticles. The observed AFM interaction can be explained by the bound magnetic polaron model for insulating diluted magnetic semiconductor systems. It is seen that the strength of AFM interaction reduces with increase in doping concentration. On the other hand, 7.5% Fe-doped SnO_2 nanoparticles show the ferromagnetic interaction, but the origin of the observed ferromagnetism is identified due to the presence of $(Fe_{1-y}Sn_y)_2O_3$ as a secondary phase.

DOI: 10.1103/PhysRevB.78.024404 PACS number(s): 75.50.Tt, 75.50.Pp, 75.30.Cr

I. INTRODUCTION

The discovery of giant magnetoresistance (GMR) (Refs. 1 and 2) in multilayer of magnetic and nonmagnetic bilayers and the theoretical model of Datta-Das field-effect transistor[3] first stimulated the scientific community to use the spin degree of freedom of electron along with its charge in electronics and born a multidisciplinary field of research, namely, spintronics.[4–6] The past 60 years after the discovery of transistor action in germanium (observed at Bell Laboratories in 1947) have the witness of revolution in semiconductor-based electronics mainly because of adding hole (+ve charge) degree of freedom of carriers in semiconductor along with electron (−ve charge). Adding further spin degree of freedom in conventional electronics is expected to be enhanced the functionality[5] of new electronic devices such as self-nonvolatile memory, low-power consumption, high speed, and large integration density compared with the conventional semiconductor devices.

Two distinct approaches are clearly observed in spintronics. One is based on the GMR effect in magnetoresistive (MR) element, which is composed of two ferromagnetic layers separated by a nonmagnetic metal or insulator and already applied successfully in practical devices such as read head,[7] spin valve,[8] magnetic random access memory,[9] and closed to realize magnetologics gates[10,11] (magnetic AND, NAND, OR, and NOR). Another approach is based on the spin injection into semiconductor either through the interface of ferromagnet/semiconductor heterostructures[12,13] or ferromagnetic ions doped into the semiconductor [dilute magnetic semiconductor (DMS) Refs. 14–16]. Although the global success of spintronics definitely depends on this approach, but the realization of practical devices is still far away.

DMS is an active field of research currently. The aim is to develop room-temperature ferromagnetism (RTFM) in conventional semiconductors by doping them with transition metals and then the DMS could be used as a host semiconductor with polarized spin carriers and/or as a spin-polarized source for heterolayered structure replacing ferromagnetic metal/insulator layer to overcome the resistance mismatch and lattice mismatch (strain) at interface. The first dilute magnetic semiconducting property was observed in intrinsically *p*-type Mn-doped GaAs (III-V semiconductor) but at quite below of room temperature around 110 K.[17] Following this work, theoretical calculations predicted the possibility of RTFM with exchange interaction mediated by *p*-type free carriers in transition-metal (TM) doped ZnO (II-VI) and GaN (III-IV) semiconductors.[18] After this prediction, a plenty number of experiments were carried out by various research groups on ZnO,[19–26] SnO_2,[27–38] and TiO_2 (Refs. 39 and 40) based DMS and reported controversial results regarding the presence or absence of ferromagnetism, regarding the origin of observed ferromagnetism whether intrinsic or due to the presence of hidden secondary phases of ferromagnetic metal clusters or their ferromagnetic oxides, regarding the exchange interactions in ferromagnetic ordering whether mediated by holes or electrons, again whether the carriers are delocalized (itinerant) or localized in nature.[15,41–46] Overall, the origin of ferromagnetism in these systems is not well understood yet.

Recently transition-metal-doped SnO_2 has been investigated by few groups and reported very high RTFM.[27–30,35–38] Being optically transparent with room-temperature ferromagnetic property, transition-metal-doped SnO_2 is considered as

a promising material for the development of multifunctional magneto-optoelectronic devices. Ogale *et al.*[30] studied $Sn_{1-x}Co_xO_2$ ($x<0.3$) thin films prepared by pulsed laser deposition (PLD) and found a strong ferromagnetic behavior at room temperature with large magnetic moment (7.5 ± 0.5 μ_B/Co). Coey *et al.*[29] studied 5% Fe-doped SnO_2 thin film grown by PLD and reported room-temperature ferromagnetism with 1.8 μ_B per ordered iron ion. Punnose *et al.*[27] and Hays *et al.*[28] observed RTFM in Fe-doped and Co-doped SnO_2 nanoparticles although the magnetic moments were significantly reduced in their nanoparticles compared to the thin films. On the contrary, Liu *et al.*[31] reported an antiferromagnetic interaction in Co-doped SnO_2 nanoparticles and Kimura *et al.*[33] observed paramagnetic behavior of Mn-doped SnO_2 thin film.

In this paper, we present our investigation to understand the structural and magnetic properties of Fe-doped SnO_2 nanoparticles prepared through a chemical coprecipitation method. The samples ($Sn_{1-x}Fe_xO_2$) were prepared with different Fe-doping concentrations ($0\leq x\leq 1$) along with pure SnO_2 ($x=0$) and Fe_2O_3 ($x=1$) nanoparticles following the identical method. We have observed that the solubility of Fe in SnO_2 is less than 7.5%. An antiferromagnetic (AFM) interaction is observed in 3% and 5% Fe-doped SnO_2 nanoparticles where the strength of AFM interaction reduces with the increase in doping concentration. However, 7.5% Fe-doped SnO_2 nanoparticles show the ferromagnetic interaction and the origin of the observed ferromagnetism is identified due to the presence of Sn-doped hematite ($(Fe_{1-y}Sn_y)_2O_3$) as a secondary phase.

II. EXPERIMENTAL DETAILS

Bulk amount of Fe-doped SnO_2 nanoparticles were prepared using a chemical coprecipitation method.[47] The intended composition was $Sn_{1-x}Fe_xO_2$ ($x=0.0$, 0.03, 0.05, 0.075, 0.1, 0.15, 0.25, 0.75, 0.90, and 1.0). 1*M* aqueous solution of $SnCl_4.5H_2O$ was mixed with 1*M* aqueous solution of $FeCl_3$ in calculated proportion of atomic percentage of Sn and Fe ions. The resulting solution was added to 1% wt/vol aqueous solution of polyvinyl pyrollidone (PVP). PVP is used as a surfactant in the reaction. The mixture was then kept in an oil bath of constant temperature of 80 °C. Initial *p*H of the solution was kept at 2.5. NH_4OH was added dropwise in a controlled manner to maintain chemical homogeneity. The addition of NH_4OH was stopped when the *p*H of the solution was reached at 8. The solution was kept under magnetic stirring for 5 hours (5 h). This reaction led to the formation of a polymeric structure within the sol particles. The sol was subsequently filtered using distilled water to eliminate chloride ions in the system and was heated at 150 °C for 1 h until completely gelled to smaller gel particles. These dry gel particles were calcined at 600 °C for 4 h to obtain the phase. The heating rate was fixed at 3.5 °C/min to reach the calcination temperature of 600 °C. XRD data were recorded at room temperature on a Phillips x-ray diffractometer with a Cu $K\alpha$ source ($\lambda=1.5418$ Å) in Bragg geometry. The loose powder samples were leveled in the sample holder to ensure a smooth surface. High-resolution transmission electron microscopy (HRTEM) measurements were carried out on a JEOL JEM 2010 microscope. All the images were digitally recorded with a slow scan charge-coupled device camera and image processing was carried out using the digital micrograph software from Gatan (USA). The HRTEM data were used for the study of particle size distribution and the crystalline character of the prepared samples. The magnetic measurements on the prepared samples were carried out using superconducting quantum interference device (SQUID) magnetometer. The temperature dependence of magnetization $[M(T)]$ and the magnetic-field dependence of magnetization $[M(H)]$ measurements were performed on the samples in the form of pressed pellets.

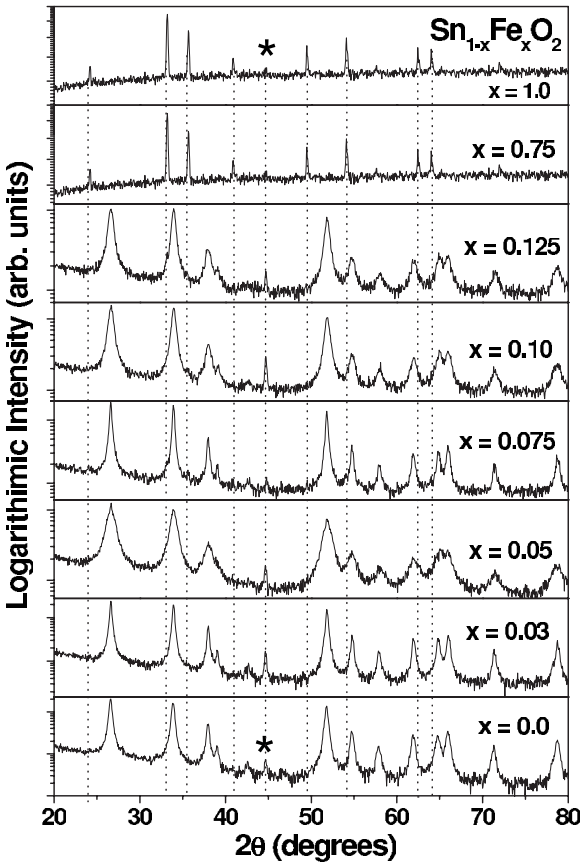

FIG. 1. Logarithmic plots of XRD data for $Sn_{1-x}Fe_xO_2$ (x=0.0, 0.03, 0.05, 0.075, 0.10, 0.120, 0.75, and 1.0) nanoparticles calcined at a temperature of 600 °C. The plots for $x=0.0$ and 1.0 indicate the XRD pattern for SnO_2 and α-Fe_2O_3, respectively. The peaks at Bragg angle 44.7° for all samples are of elemental Mn atoms from sample holder of XRD machine (marked with *).

III. RESULTS AND DISCUSSIONS

A. Structural

We have shown powder XRD patterns of $Sn_{1-x}Fe_xO_2$ ($x=0.03$, 0.05, 0.075, 0.10, 0.125, and 0.75) nanoparticles in Fig. 1 along with pure SnO_2 ($x=0.0$) and Fe_2O_3 ($x=1.0$) nanoparticles prepared under identical conditions for the identification of the phases in $Sn_{1-x}Fe_xO_2$. The experiment

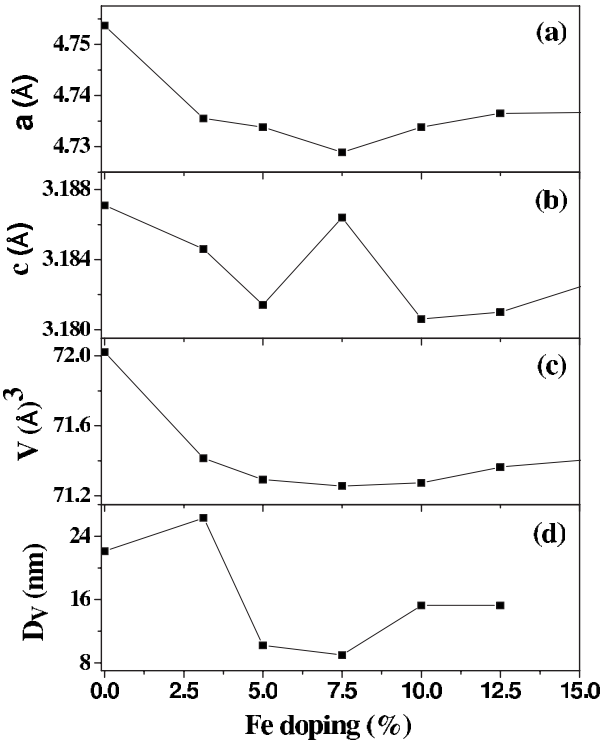

FIG. 2. Variation of (a) lattice parameter a, (b) lattice parameter c, (c) cell volume V (a^2c), and (d) crystallite size in diameter D_V calculated from XRD peaks of (110) and (101) shown in Fig. 1.

was performed with bulk amount of material and the intensity of the Bragg peaks is plotted in the logarithmic scale to enhance the sensitivity of XRD in detection of the presence of tiny amount of secondary phases. Figure 1 shows that $Sn_{1-x}Fe_xO_2$ have the identical structure of SnO_2 up to Fe-doping concentration of $x=0.125$ beyond which the additional peaks start to appear at Bragg angles of Fe_2O_3. The XRD patterns of SnO_2 and Fe_2O_3 are compared with the JCDPS software generated XRD patterns and it is found that SnO_2 is cassiterite phase (tetragonal phase with no orthorhombic phase is observed) and Fe_2O_3 is hematite phase (hexagonal). It is observed that there is a competition to form Fe-substituted SnO_2 phase and/or Sn-substituted Fe_2O_3 phase depending on the relative concentration of Sn and Fe ions. Below (above) 25% (75%) of Fe concentration, Fe-substituted SnO_2 (Sn-substituted Fe_2O_3) is the dominant phase. From Fig. 1, it is evident that 75% Fe-doped samples have the identical structure of Fe_2O_3. So the secondary phases, in our case, may be Fe_2O_3 and/or Sn-substituted Fe_2O_3 $[(Fe_{1-y}Sn_y)_2O_3]$. Note that a peak at a Bragg angle of 44.7° in Fig. 1 appears for all samples ($x=0.0$ to $x=1.0$), which is the peak of elemental Mn atoms (not any Mn oxide) from the sample holder of XRD machine.

Lattice parameters (a and c), cell volume (a^2c), and particle size (D_V) were calculated using the casseterite (110) and (101) peaks of $Sn_{1-x}Fe_xO_2$ for different doping concentrations (x) and their average values are plotted in Fig. 2. Lattice parameters (a and c) and cell volume gradually decrease with the increase in doping concentration and reaches a minimum at doping level of ~7.5% and increase with further rise in the doping concentration. Lattice parameter c at ~7.5% is

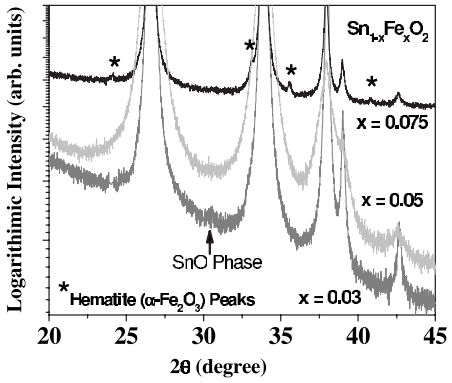

FIG. 3. HRXRD of 3%, 5%, and 7.5% Fe-doped SnO_2 nanoparticles showing the presence of secondary hematite phase (α-Fe_2O_3) in 7.5% Fe-doped sample. The very weak peak at Bragg angle of 30.2° is for the tetragonal phase of SnO (marked with arrow). Peaks at 44.7° are absent because of using different sample holder in HRXRD machine.

deviated from the trend and the reason is not clear. It is noted that the calculation is repeatedly checked and obtained the same result. From Fig. 2 it is clear that the structural change in $Sn_{1-x}Fe_xO_2$ is distinctly different below and above the doping concentration of 7.5%. The lattice parameters (a and c) and cell volume (a^2c) decreases up to doping concentration of 7.5% and for higher concentration the same increases toward the value of pure SnO_2. The ionic radii of O^{2-}, Sn^{4+}, and Fe^{3+} are 1.40, 0.83, and 0.69 Å, respectively. Obviously the radius of dopant ion (Fe^{3+}) is lower than that of host ion (Sn^{4+}). It may happen that Fe atoms are incorporated into SnO_2 matrix at substitutional and/or interstitial position below 7.5% and then started to segregate for higher concentration and manifest as a secondary phase. We have also calculated the crystallite size using the Scherrer formula,[48]

$$D_v = \frac{K\lambda}{\beta_{1/2}\cos\theta}, \tag{1}$$

where θ is the Bragg angle and $\beta_{1/2}$ is the full width at half maxima, $\lambda=1.5418$ Å in the Cu $K\alpha$ radiation. K is taken to be 0.89. The dependence of the crystallite size with doping concentration is shown in Fig. 2(d), which shows a similar trend as the other structural parameters with a significant critical point at doping concentration of 7.5%. Further, we have performed the high-resolution x-ray diffraction (HRXRD) (lower angle step, higher incident intensity, and longer scan time) measurements on the samples doping with 3%, 5%, and 7.5% Fe and shown the results in Fig. 3. The plots in Fig. 3 establish the evolution of secondary phases just started at 7.5% below which $Sn_{1-x}Fe_xO_2$ is single phase with identical structure of SnO_2. Thus the solubility of Fe in SnO_2 at 600 °C is less than 7.5%. In Fig. 3, a very weak peak at Bragg angle 30.2° for 3% Fe-doped sample is resolved in HRXRD, which is identified as the peak of the tetragonal phase of SnO. However, the relative intensity of the peak is so low that the presence of SnO phase is negligibly small compared to the SnO_2 phase. Further, the absence of peak at 44.7° (identified in Fig. 1 as the peak of

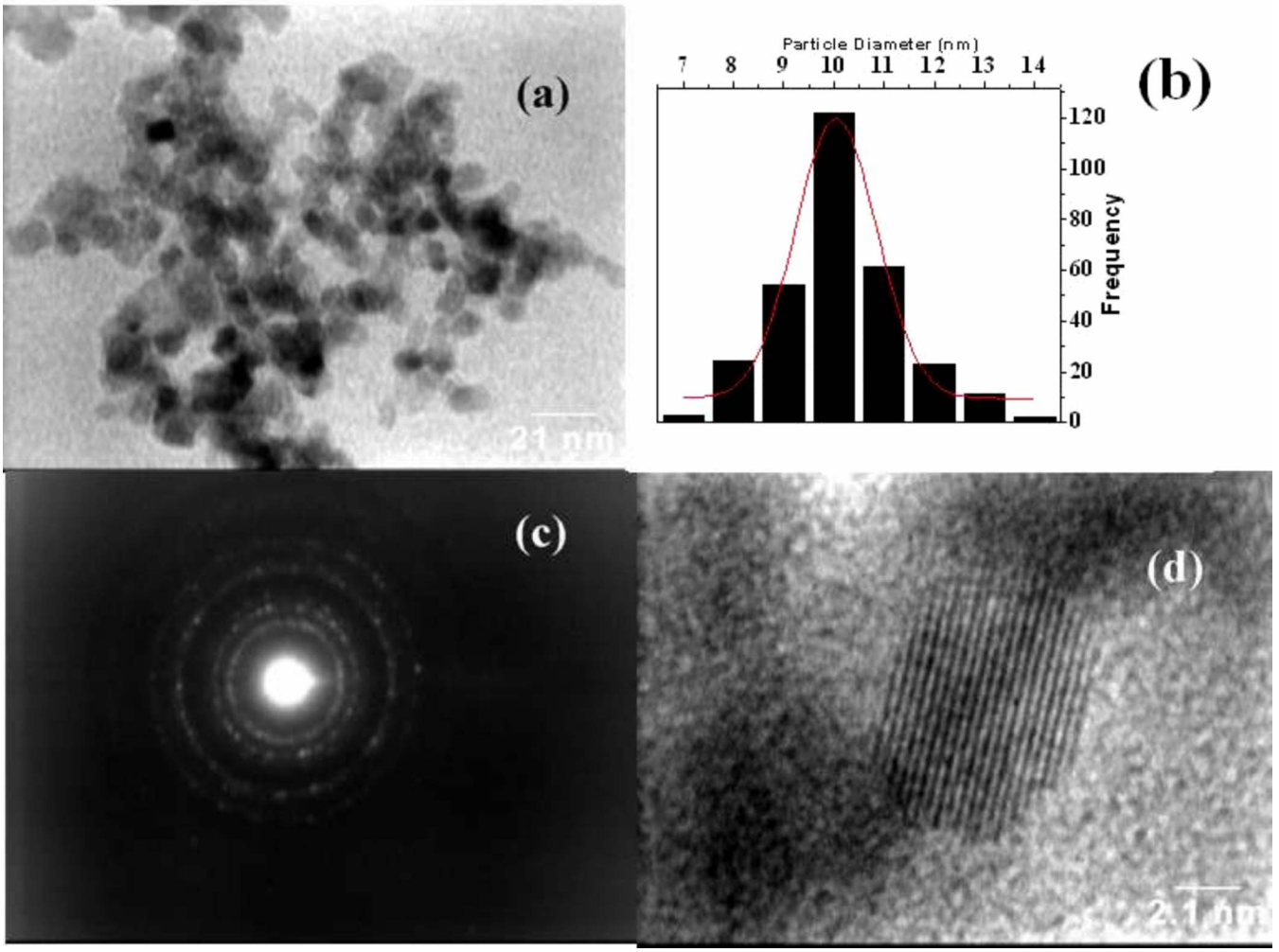

FIG. 4. (Color online) (a) Low magnification TEM image, (b) Particle size distribution determined from (a), (c) SAD pattern, and (d) Lattice image (HRTEM) of $Sn_{0.95}Fe_{0.05}O_2$ nanoparticles calcined at 600 °C (see text for details).

elemental Mn atoms from sample holder) in Fig. 3 of HRXRD pattern (which was recorded in different machine) confirms that the source of Mn peak is the sample holder of XRD machine.

Structural characterization through TEM is a direct way of visualizing the estimated grain size. It also gives authentic information regarding the particle size distribution, crystalline nature, and other structural information. Figure 4(a) shows the low magnification TEM micrograph of $Sn_{0.95}Fe_{0.05}O_2$ nanoparticles synthesized at calcination temperature of 600 °C. From this micrograph, the particle size is determined and shown in Fig. 4(b). It is found that the particles are distributed with maximum frequency at ~10 nm, which is very consistent with the XRD analysis [Fig. 2(d)]. The particle size (diameter) was edited, analyzed, and calculated using the ADOBE PHOTOSHOP and IMAGE J software, respectively. The average particle size for other concentrations was also found to be markedly consistent with the values obtained from XRD analysis. The selected area diffraction (SAD) pattern shown in Fig. 4(c) demonstrates that the particles are crystalline in nature. The concentric ring in SAD pattern may not be due to the polycrystalline nature of the individual particles, rather random orientation of particles in powder form. However HRTEM images of the $Sn_{0.95}Fe_{0.05}O_2$ nanoparticles [shown in Fig. 4(d)] confirmed that the particles are single crystalline and almost free from the defects. We have observed that there is no formation of any structural core-shell system. However, the HRTEM analysis could not quantitatively conclude the evolution of any secondary phases in samples even with higher doping concentration of Fe ($x > 0.05$). The elemental analysis from energy dispersive x-ray analysis measurements showed a close match with our intended material composition as stated in the synthesis process (data are not shown here).

B. Magnetic

For proper investigation and understanding of the magnetic properties of $Sn_{1-x}Fe_xO_2$ ($x=0.03$, 0.05, and 0.075) DMS nanoparticles, measurements of magnetization as a function of temperature [$M(T)$] and magnetic field [$M(H)$] were carried out over a temperature range of 5–300 K and field range of 0 to ±5 kOe using a SQUID magnetometer. Figure 5 shows the M-H behavior of 3%, 5%, and 7.5% Fe-doped SnO_2 nanoparticles. 3% [Fig. 5(a)] and 5% [Fig. 5(b)] Fe-doping samples do not show any hysteresis loop in

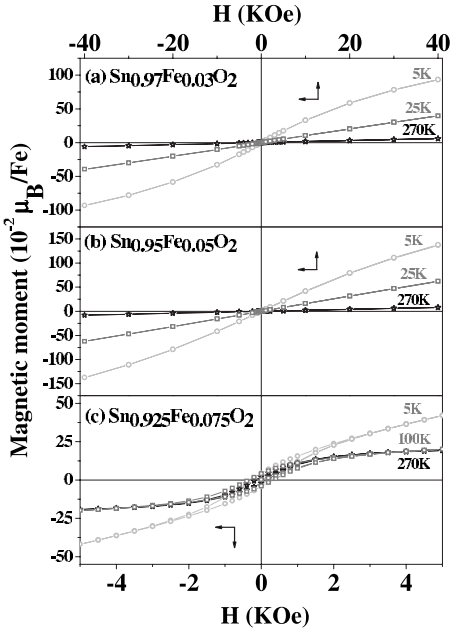

FIG. 5. $M(H)$ plots for (a) $Sn_{0.97}Fe_{0.03}O_2$, (b) $Sn_{0.95}Fe_{0.05}O_2$, and (c) $Sn_{0.0925}Fe_{0.075}O_2$ at different temperatures.

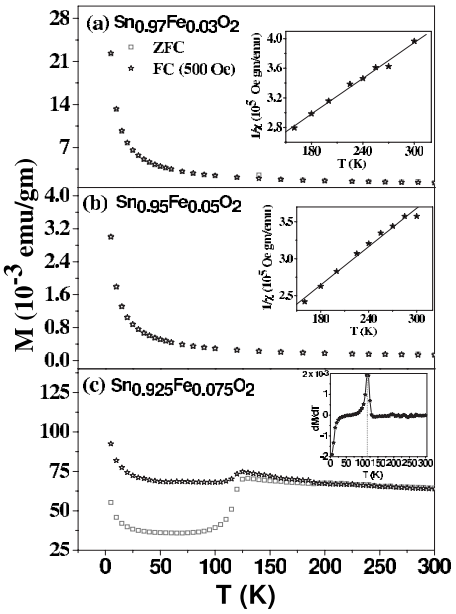

FIG. 6. $M(T)$ plots for (a) $Sn_{0.97}Fe_{0.03}O_2$, (b) $Sn_{0.95}Fe_{0.05}O_2$ [inset (a) and (b) showing the high-temperature Curie-Weiss fit of the inverse susceptibility $(1/\chi)$-temperature (T) plot from the $M(T)$ data], and (c) $Sn_{0.0925}Fe_{0.075}O_2$ (inset showing the dM/dT vs T plot, clearly depicting the Morin transition) with $H=500$ Oe (FC) and $H=0$ Oe (ZFC).

the whole range of temperature (5–300 K), but the 7.5% [Fig. 5(c)] sample shows. Obviously 3% and 5% samples are not ferromagnetic and also not superparamagnetic for lacking of magnetization saturation even at higher magnetic field. There is only possibility to be either paramagnetic or antiferromagnetic. On the other hand, 7.5% sample is obviously ferromagnetic in nature and now the question is to be answered whether this observed ferromagnetism is intrinsic property of Fe-substituted SnO_2 or due to the secondary phase predicted from HRXRD. Note that the normal XRD could not detect the presence of secondary phase and hysteretic behavior of 7.5% Fe-doped sample might tempt one to conclude that the observed ferromagnetism would be intrinsic phenomenon of Fe-substituted SnO_2. The $M(T)$ curves for $Sn_{1-x}Fe_xO_2$ ($x=0.03$, 0.05, and 0.075) samples in the presence of a dc magnetic field of 500 Oe [field cooled (FC)] and in the absence of magnetic field [zero field cooled (ZFC)] are shown in Fig. 6. The $M(T)$ curves for $x=0.03$ [Fig. 6(a)] and $x=0.05$ [Fig. 6(b)] show a steep rise in magnetization value with a very strong concave nature below 50 K without any distinct magnetic phase transition. It is also observed that the concave nature of $M(T)$ curves decreases with increase of Fe doping from 3% to 5% in the SnO_2 matrix. The FC and ZFC curves for the lower Fe-doped samples i.e., for the 3% and 5% samples coincide (as shown in figure with separate symbols), indicating an antiferromagnetic interaction among the magnetic ions in the matrix without any spin-glass-type transition. Similar observations have been reported by Liu *et al.*[31] for Co doped SnO_2 nanoparticles prepared from a similar coprecipitation method. The $M(T)$ curves for the 7.5% Fe-doped sample [shown in Fig. 6(c)] are very different, where FC and ZFC curves separate out at a temperature of ~190 K and a magnetic phase transformation occurs steadily between 125 and 95 K (see ZFC curve). This transformation is easily identified at the first look to be a transformation from a weak ferromagnetic (WFM) phase to an AFM phase. It looks also that this magnetic phase transformation is superimposed with the interaction dominating in the samples of lower Fe concentration (3% and 5%), which is evident from the strong concavity in the FC and ZFC curves at lower temperature, a marked similarity with the lower doping samples [Fig. 6(a) and 6(b)]. It is reported in literature that hematite shows a similar phase transformation from a WFM to AFM at temperature of 263 K called the Morin transition temperature T_M.[49] In our case, the observed transition at temperature of 113 K with asymmetric width of 30 K [see inset in Fig. 6(c)] may be due to the Morin transition of secondary phase (hematite). However, $M(H)$ and $M(T)$ curves together clearly support the single (primary) phase nature of 3% and 5% samples and the multiphase (primary and secondary) nature of 7.5% sample as observed in HRXRD results. A schematic diagram decoupling the contribution of each phase in $M(T)$ for 7.5% sample are shown in Fig. 7. For a quantitative evaluation of the intrinsic exchange coupling between Fe ions in SnO_2 matrix for 3% and 5% samples and to identify the origin of ferromagnetic component in 7.5% Fe-doped sample, we discuss them separately as follows.

1. 3% and 5% Fe-doped SnO_2

The plots of magnetization (M) as a function of temperature (T) are shown in Figs. 6(a) and 6(b) for 3% and 5% Fe-doped SnO_2, respectively. The inverse susceptibility $(1/\chi)$ versus T are fitted with a Curie-Weiss linear relation for the high-temperature regime (shown as inset),

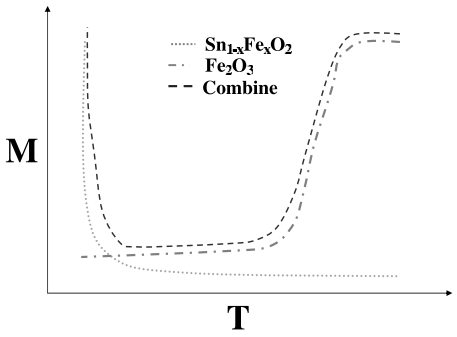

FIG. 7. Schematic of the possible interaction for the observed peculiarity in *M-T* nature of 7.5% Fe-doped SnO_2 sample.

$$[\chi(x)]^{-1} = \frac{\{T - \theta(x)\}}{C(x)}, \tag{2}$$

where $\theta(x)$ is the Curie-Weiss temperature and $C(x)$ is the Curie constant. $\theta(x)$ is estimated from the linear fit of the experimental curves. The magnitude of $\theta(x)$ is found to be ~ -128 K for $x=0.03$ and -146 K for $x=0.05$. Thus the magnetic interaction in this system is found to be antiferromagnetic in nature as estimated from the negative value of $\theta(x)$. Such AFM interaction was also found for Co and Mn-doped ZnO systems.[19,20] The effective Bohr magneton is calculated from the slope $C(x)$ of the linear Curie-Weiss fit through the relation[50]

$$\mu_{\text{eff}} = \left[\frac{3k_B C(x)}{N_A}\right], \tag{3}$$

where k_B is the Boltzmann constant and N_A is the Avogadro number. Again,

$$\mu_{\text{eff}} = g\{J(J+1)\}^{1/2}\mu_B, \tag{4}$$

where μ_B is the Bohr magneton number and g is the Lande-g factor, which we take as 2.023 for Fe ion.[50] The calculated values of J, μ_{eff}, $C(x)$ and $\theta(x)$ for $Sn_{0.97}Fe_{0.03}O_2$ and $Sn_{0.95}Fe_{0.05}O_2$ are tabulated in Table I. The AFM interaction of $Sn_{0.97}Fe_{0.03}O_2$ and $Sn_{0.95}Fe_{0.05}O_2$ can be understood well if we calculate the effective exchange interaction parameter J_{ex} using the relation

$$J_{ex} = \frac{3\theta(x)k_B}{xJ(J+1)Z_{NN}}, \tag{5}$$

where x is the atomic fraction of the magnetic ions in the matrix and Z_{NN} (=14) is the number of nearest neighbor for the system. Using the parameters calculated in Table I, the values of J_{ex}/k_B are found as -308.23 K for $Sn_{0.97}Fe_{0.03}O_2$ and -259.26 K for $Sn_{0.95}Fe_{0.05}O_2$. The negative sign of the parameter J_{ex}/k_B confirms our inference regarding the AFM-type interaction in the 3% and 5% doped SnO_2 nanoparticles. The magnitude of the strength of the AFM interaction in $Sn_{1-x}Fe_xO_2$ nanoparticles with a growth temperature of 600 °C is found to be decreased with the increase in Fe^{3+} concentration in the matrix.

The concavity in $M(T)$ is a signature for small free-carrier density and small mean free path, while convex profiles appear for the large and linear for the intermediate density and mean free path. The strong concave nature of $M(T)$ curves in our Fe-doped SnO_2 nanometric samples is clearly suggesting a strongly localized nature of the magnetic ions and a "low-value" carrier density insulating system.[44,45] According to Bhatt *et al.*,[46] the temperature dependence of magnetic susceptibility on donor-rich n-doped semiconductors (electrically insulating) shows the absence of any ferromagnetic ordering due to AFM exchange coupling between donor spins down to very low temperature ~ 10 mK. Though the doping of SnO_2 by Fe^{3+}, where Fe^{3+} is intended to substitute Sn^{4+} ions, would effectively give rise to a hole dominated system, but the inherent anionic defects and deficiencies along with the enhanced grain-boundary effects in these nanometric materials may give it a insulating nature. The observed magnetic behavior in our sample can be explained by considering the bound magnetic polaron (BMP) model.[43,44] The anionic defects or the localized carrier along with the magnetic impurity spin are likely to form a BMP in the present system of Fe-doped SnO_2, where one localized carrier is surrounded by many magnetic impurity spins with net magnetic moment. Such BMPs are distributed throughout the system randomly along some magnetic ion species. According to Wolff *et al.*,[43] three types of interactions are present among the BMPs, viz., (i) K, the kinetic exchange interaction between the spin of the localized carrier and spin of the magnetic impurities within the magnetic polaron; (ii) K', the polaron-polaron coupling induced through an exchange via the magnetic ions residing between the magnetic polarons; and (iii) J, the standard AFM interaction induced by virtual hopping of carriers from one site to another. In our work, the doping concentrations are in higher TM doping level and we can consider $(a^*/d) \geq 1$, where a^* is the effective Bohr radius for the magnetic polaron and d is the distance between two such BMPs.[43] Because of the limit of $(a^*/d) \geq 1$ in such systems, K' and J are not negligible to be treated as second-order perturbations and different degrees of competitions between these two interaction parameters arise. For $K'/J=0$, there is no competition and we have an AFM interaction. An increase in value of this K'/J term would mean a gradual relaxation of the AFM interaction in the system. This relaxation of the

TABLE I. Comparison of $C(x)$, effective Bohr magneton (μ_{eff}), total angular quantum number J, Neel temperature $\theta(x)$, and magnitude of AFM interaction strength (J_{ex}/k_B) for $Sn_{0.97}Fe_{0.03}O_2$ and $Sn_{0.95}Fe_{0.05}O_2$.

Sample	$C(x)$	$\mu_{\text{eff}}(x\mu_B)$	J	$\theta(x)$ (K)	J_{ex}/k_B (K)
$Sn_{0.97}Fe_{0.03}O_2$	0.00112	1.1446	1.26	−128	−308.23
$Sn_{0.95}Fe_{0.05}O_2$	0.001244	0.3555	1.132	−146	−259.26

AFM interaction is indeed observed in our system as we increase the doping concentration. Since an increase in the doping concentration would mean an increase in the effective number of Fe ions in the matrix, thus the effective Bohr radius of the magnetic polarons increase and as such K' increases as K' is related to parameter K by $K' \sim K \exp(-d/a^*)$. However, interestingly the magnetic interaction in our Fe-doped SnO_2 is never ferromagnetic though Punnose *et al.*[27] reported a RTFM in 1% Fe-doped SnO_2 nanoparticles with a lower growth temperature. In their studies the samples grown at 600 °C did not show any ferromagnetism. This can be attributed to the fact that due to the increased growth temperature, there is a surface diffusion of the magnetic ions. Comparably the generation of the anionic defects and other defects also appear that prefer the formation of the BMPs with competing interaction parameters, viz., K' and J. The reason is attributed to the fact that with the increase of Fe ions in the matrix, the number of antiferromagnetically interacting magnetic polaronic pairs also increase. So there will be a net decrease in the strength of the AFM exchange interaction due to the increased value of the parameter K' and effectively the K'/J value for modifications in a^* and simultaneously the moment per Fe ions should reduce with increase in the AFM exchange sites.

2. 7.5% *Fe-doped* SnO_2

A marked difference is observed in the $M(H)$ [Fig. 5(c)] and $M(T)$ [Fig. 6(c)] curves for 7.5% Fe-doped sample in comparison with the same of 3% and 5% Fe-doped samples. In contrast to the lower doping (3% and 5%) samples, the 7.5% sample shows (i) hysteresis loop at lowest attainable temperature of 5 K and also at higher temperature of 270 K and (ii) phase transition from WFM to AFM starting at ~125 K over a range of temperature down to 95 K. This behavior in the 7.5% Fe-doped sample is attributed at the first hand due to the presence of secondary α-Fe_2O_3 phase. To understand this different $M(H,T)$ behavior, we have measured the magnetization of α-Fe_2O_3 nanoparticles (prepared by the similar coprecipitation method as described earlier) both as functions of temperature and magnetic field, as shown in Fig. 8. The following observations are made from the $M(H,T)$ curves of α-Fe_2O_3 nanoparticles: (i) hysteresis loop at 5 K is absent but present at 270 K, and (ii) phase transition from WFM to AFM starting at ~260 K over a range of temperature down to 200 K is present. The observed phase transition is definitely the Morin transition where the antiferromagnetically aligned Fe spins of α-Fe_2O_3 are slightly canted below its Néel temperature of 960 K and attains the perfect antiparallel orientation below the Morin temperature (T_M) of 263 K in case of bulk material. In our sample, the wide range of T_M (ΔT_M=60 K) is attributed to the effect of size distribution of α-Fe_2O_3 nanoparticles and evidence of such effect is found in literatures.[49,51–55] Also the absence of hysteresis loop at 5 K is expected since 5 K is quite below the observed Morin temperature of 255 K (see inset) in our sample of α-Fe_2O_3 nanoparticles. Note that the secondary phases in 7.5% sample and pure α-Fe_2O_3 nanoparticles show similar behavior with the following differences: (i) the Morin transition in 7.5% sample is at 113 K whereas in pure α-Fe_2O_3 nanoparticles, the same is at 255 K, and (ii) 7.5% sample shows hysteresis at 5 K, but pure α-Fe_2O_3 nanoparticles do not show the same. This difference may not be only due to the particle size effect on Morin transition. Also the substitution of Sn^{4+} ions in place of the Fe^{3+} cations in the α-Fe_2O_3 rhombohedral structure might be a possible reason for this lowering of the Morin temperature. Suppression of Morin transition temperatures in Ti-, Al-, Co-, Sn-, and Mn-doped hematites is reported in literatures.[55–60] We have also noted that Sn when doped in α-Fe_2O_3 is structurally identical to that of α-Fe_2O_3 (compare XRD plots of 75% and 100% Fe-doped samples in Fig. 1). Here we mean that 75% and 100% Fe-doped SnO_2 is equivalent to 25% and 0% Sn-doped α-Fe_2O_3. Our intuition is that the possible presence of a phase of the form α-$(Fe_{1-y}Sn_y)_2O_3$ is responsible for the observation of the hysterisis at 5 K. To confirm our intuition, we have measured $M(H,T)$ of 75% Fe-doped SnO_2 sample and shown the data in Fig. 9. XRD shows that this sample is mainly Sn-substituted α-Fe_2O_3 phase (Fig. 1) and this phase shows hysteresis loop at 5 K [Fig. 9(a)] and the Morin transition temperature is less than 5 K [Fig. 9(b)]. However, the appearance of hysteresis loop at 5 K is still not clear when the Morin transition temperature is 113 K with a range of 125–95 K in 7.5% Fe-doped sample. Moreover, the presence of the ferromagnetic magnetite phase is discarded as the high air annealing temperature of ~600 °C of the samples will not allow this phase to be stable and magnetite gets oxidized to Fe_2O_3 (maghemite and subsequently hematite) phase at annealing temperatures ~300 °C. It is reported recently by Xu *et al.*[53] that chemically hematite nanowires exhibit a T_M below 4 K and has a hysteretic behavior even at low temperatures of 10 K. We attribute the presence of hysterisis at 5 K in 7.5% Fe-doped

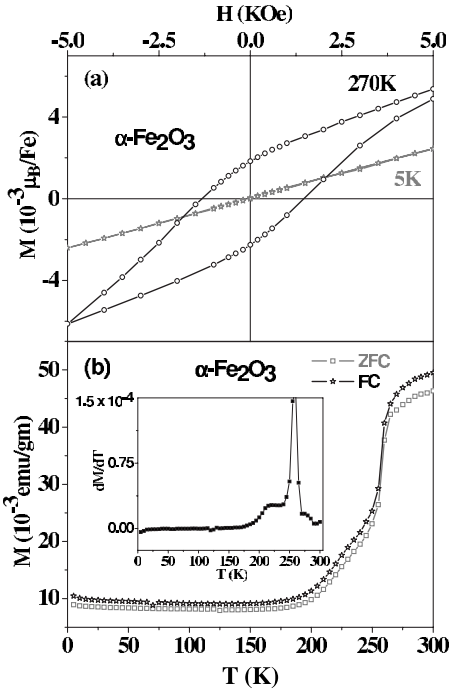

FIG. 8. (a) M-H plot at 5 and 270 K and (b) M-T curve with H=500 Oe (FC) and H=0 Oe (ZFC) for α-Fe_2O_3.

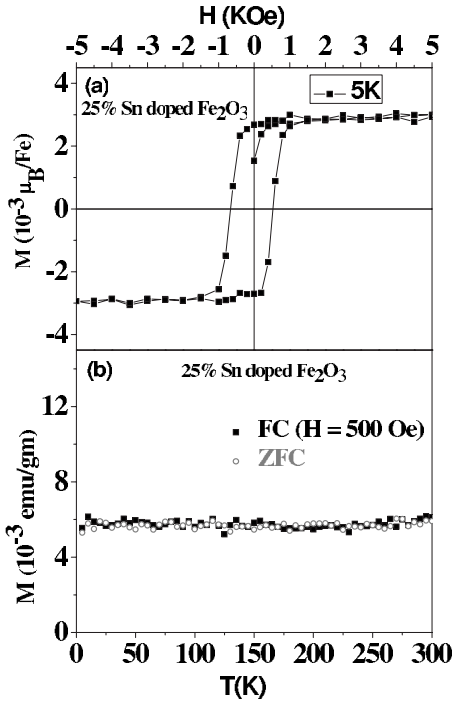

FIG. 9. (a) M-H plot at 5 K and (b) M-T curve at $H=500$ Oe (FC) and $H=0$ Oe (ZFC) for 25% Sn-doped α-Fe_2O_3.

sample due to the inhomogeneous Sn-substitution into Fe_2O_3 and also size and shape distribution of the particles.

IV. SUMMARY

We have synthesized Fe-doped SnO_2 nanoparticles by a coprecipitation method. The prepared samples with Fe-doping percentage varying from 3% to 75% showed a SnO_2 casseterite phase up to a doping percentage of 7.5% as concluded from the normal XRD analysis. However HRXRD studies showed the presence of a secondary phase α-Fe_2O_3 in the 7.5% Fe-doped SnO_2 sample. Further structural analysis of the obtained XRD spectra shows that the lattice parameter and cell volume changes in accordance with the incorporation of Fe ions into the SnO_2 matrix. For higher Fe doping the lattice parameters approaches the undoped SnO_2 suggesting segregation of Fe as oxides [α-Fe_2O_3 and α-$(Fe_{1-y}Sn_y)_2O_3$ in this case]. The crystallite size calculated from the Scherer formula suggests the formation of nanometric particles which is further confirmed by the HRTEM images. The single crystalline and defect free nature of the particles are also evident from HRTEM images. The magnetic behavior of the single phase system, i.e., for the 3% and 5% Fe-doped SnO_2 samples that showed an AFM behavior, which is explained through the BMP model. Though the system exhibits a non-mean–field-like behavior, but we have used the Curie-Weiss model to describe the $M(T)$ behavior. This is justified as we try to get a qualitative quantification of the exchange parameters governing the magnetic behavior of the single phase $Sn_{1-x}Fe_xO_2$ system. The next-higher concentration, i.e., 7.5% Fe-doped sample showed the presence of α-Fe_2O_3 as a secondary phase, and the magnetic behavior, viz., $M(T)$ and $M(H)$ indicated a coupled behavior of individual α-Fe_2O_3 phase and the $Sn(Fe)O_2$ phase as evident from the observed Morin transition from a WFM phase to an AFM phase in the system. However, the Morin temperature is shifted to much lower temperature $\sim$100 K for the 7.5% Fe-doped sample, a marked departure from that of pure α-Fe_2O_3 ($T_M \sim 255$ K). Also the existence of hysteresis at 5 K indicates that the secondary phase evolved in the 7.5% sample is not strictly pure α-Fe_2O_3 but a Sn-substituted α-Fe_2O_3 phase that we propose as α-$(Fe_{1-y}Sn_y)_2O_3$. This conclusion is further supported by the $M(H)$ and $M(T)$ studies on the 75% Fe-doped SnO_2 sample, which is structurally identical to α-Fe_2O_3. The $M(T)$ plot clearly suggest the disappearance of the Morin transition and a profound hysteresis at 5 K suggest the weak ferromagnetic nature of the α-$(Fe_{1-y}Sn_y)_2O_3$ phase. Further investigation is needed to study the behavior of Fe-doped SnO_2 system prepared at a lower temperature $\sim$300 K and relatively lower doping ($<3\%$) concentration of Fe in the SnO_2 matrix.

ACKNOWLEDGMENTS

We are grateful to G. P. Das for his encouragement and active support for this work. We also acknowledge active support of P. V. Satyam for TEM measurements. We acknowledge the financial support of BRNS India (Project No. 2006/37/29/BRNS/1166) and CSIR India [Project No. 03(1017)/05/EMR-II] for this work.

*Corresponding author. FAX: +91-3222-282700; email: amal@phy.iitkgp.ernet.in

[1] M. N. Baibich, J. M. Broto, A. Fert, F. Nguyen Van Dau, F. Petroff, P. Etienne, G. Creuzet, A. Friederich, and J. Chazelas, Phys. Rev. Lett. **61**, 2472 (1988).

[2] G. Binasch, P. Grunberg, F. Saurenbach, and W. Zinn, Phys. Rev. B **39**, 4828 (1989).

[3] Supriyo Datta and Biswajit Das, Appl. Phys. Lett. **56**, 665 (1990).

[4] G. A. Prinz, Science **282**, 1660 (1998).

[5] S. A. Wolf, D. D. Awschalom, R. A. Buhrman, J. M. Daughton, S. von Molnar, M. L. Roukes, A. Y. Chtchelkanova, and D. M. Treger, Science **294**, 1488 (2001).

[6] Igor Žutic, Jaroslav Fabian, and S. Das Sarma, Rev. Mod. Phys. **76**, 323 (2004).

[7] Wall Street Journal, 10 November 1997, p. 88.

[8] J. M. Daughton, J. Brown, R. Beech, A. Pohm, and W. Kude, IEEE Trans. Magn. **30**, 4608 (1994).

[9] http://www.motorola.com/mediacenter/news/

[10] C. Pampuch, A. K. Das, A. Ney, L. Daweritz, R. Koch, and K. H. Ploog, Phys. Rev. Lett. **91**, 147203 (2003).

[11] A. Ney, C. Pampuch, R. Koch, and K. H. Ploog, Nature (Lon-

don) **425**, 485 (2003).
[12] H. J. Zhu, M. Ramsteiner, H. Kostial, M. Wassermeier, H.-P. Schönherr, and K. H. Ploog, Phys. Rev. Lett. **87**, 016601 (2001).
[13] M. Ramsteiner, H. Y. Hao, A. Kawaharazuka, H. J. Zhu, M. Kästner, R. Hey, L. Däweritz, H. T. Grahn, and K. H. Ploog, Phys. Rev. B **66**, 081304(R) (2002).
[14] J. K. Furdyna, J. Appl. Phys. **64**, R29 (1988).
[15] H. Ohno, Science **281**, 951 (1998).
[16] S. J. Pearton, C. R. Abernathy, M. E. Overberg, G. T. Thaler, D. P. Norton, N. Theodoropoulou, A. F. Hebard, Y. D. Park, F. Ren, J. Kim, and L. A. Boatner, J. Appl. Phys. **93**, 1 (2003).
[17] F. Matsukura, H. Ohno, A. Shen, and Y. Sugawara, Phys. Rev. B **57**, R2037 (1998).
[18] T. Dietl, H. Ohno, F. Matsukura, J. Cibert, and D. Ferrand, Science **287**, 1019 (2000).
[19] S. K. Mandal, A. K. Das, T. K. Nath, Debjani Karmakar, and B. Satpati, J. Appl. Phys. **100**, 104315 (2006).
[20] S. K. Mandal, T. K. Nath, A. K. Das, and Debjani Karmakar, Appl. Phys. Lett. **89**, 144105 (2006); J. Appl. Phys. **101**, 063913 (2007).
[21] A. S. Risbud, N. A. Spaldin, Z. Q. Chen, S. Stemmer, and Ram Seshadri, Phys. Rev. B **68**, 205202 (2003).
[22] S. Yin, M. X. Xu, L. Yang, J. F. Liu, H. Rösner, H. Hahn, H. Gleiter, D. Schild, S. Doyle, T. Liu, T. D. Hu, E. Takayama-Muromachi, and J. Z. Jiang, Phys. Rev. B **73**, 224408 (2006).
[23] S. Kolesnik, B. Dabrowski, and J. Mais, J. Supercond. **15**, 251 (2002).
[24] S. J. Han, T.-H. Jang, Y. K. Kim, B. G. Park, J.-H. Park, and J. H. Jeong, Appl. Phys. Lett. **83**, 920 (2003).
[25] Debjani Karmakar, S. K. Mandal, R. M. Kadam, P. L. Paulose, A. K. Rajarajan, T. K. Nath, A. K. Das, I. Dasgupta, and G. P. Das, Phys. Rev. B **75**, 144404 (2007).
[26] J. Hays, A. Thurber, K. M. Reddy, A. Punnose, and M. H. Engelhard, J. Appl. Phys. **99**, 08M123 (2006).
[27] A. Punnoose, J. Hays, A. Thurber, M. H. Engelhard, R. K. Kukkadapu, C. Wang, V. Shutthanandan, and S. Thevuthasan, Phys. Rev. B **72**, 054402 (2005).
[28] J. Hays, A. Punnoose, R. Baldner, M. H. Engelhard, J. Peloquin, and K. M. Reddy, Phys. Rev. B **72**, 075203 (2005).
[29] J. M. D. Coey, A. P. Douralis, C. B. Fitzgerald, and M. Venkatesan, Appl. Phys. Lett. **84**, 1332 (2004).
[30] S. B. Ogale, R. J. Choudhary, J. P. Buban, S. E. Lofland, S. R. Shinde, S. N. Kale, V. N. Kulkarni, J. Higgins, C. Lanci, J. R. Simpson, N. D. Browning, S. Das Sarma, H. D. Drew, R. L. Greene, and T. Venkatesan, Phys. Rev. Lett. **91**, 077205 (2003).
[31] C. M. Liu, X. T. Zu, and W. L. Zhou, J. Phys.: Condens. Matter **18**, 6001 (2006).
[32] A. Thurber, J. Hays, K. M. Reddy, V. Shutthanandan, and A. Punnose, J. Mater. Sci.: Mater. Electron. **18**, 1151 (2007).
[33] H. Kimura, T. Fukumura, M. Kawasaki, K. Inaba, T. Hasegawa, and H. Koinima, Appl. Phys. Lett. **80**, 94 (2002).
[34] J. F. Liu, M. F. Lu, P. Chai, L. Fu, Z. L. Wang, X. Q. Cao, and J. Meng, J. Magn. Magn. Mater. **317**, 1 (2007).
[35] W. Wang, Z. Wang, Y. Hong, J. Tang, and M. Yu, J. Appl. Phys. **99**, 08M115 (2006).
[36] K. Nomura, C. A. Barrero, J. Sakuma, and M. Takeda, Phys. Rev. B **75**, 184411 (2007).
[37] C. B. Fitzgerald, M. Venkatesan, L. S. Dorneles, R. Gunning, P. Stamenov, J. M. D. Coey, P. A. Stampe, R. J. Kennedy, E. C. Moreira, and U. S. Sias, Phys. Rev. B **74**, 115307 (2006).
[38] A. Punnoose, J. Hays, V. Gopal, and V. Shutthanandan, Appl. Phys. Lett. **85**, 1559 (2004).
[39] Y. Matsumoto, M. Murakami, T. Shono, and T. Hasegawa, Science **291**, 854 (2001).
[40] K. M. Reddy and A. Punnose, J. Appl. Phys. **101**, 09H112 (2007); J. Mater. Sci.: Mater. Electron. **18**, 1197 (2007).
[41] Mona Berciu and R. N. Bhatt, Phys. Rev. Lett. **87**, 107203 (2001).
[42] A. Kaminski and S. Das Sarma, Phys. Rev. Lett. **88**, 247202 (2002).
[43] P. A. Wolff, R. N. Bhatt, and A. C. Durnst, J. Appl. Phys. **79**, 5196 (1996).
[44] M. J. Calderón and S. Das Sarma, Ann. Phys. **322**, 2618 (2007).
[45] S. Das Sarma, E. H. Hwang, and A. Kaminski, Phys. Rev. B **67**, 155201 (2003).
[46] R. N. Bhatt, Phys. Rev. Lett. **48**, 707 (1982).
[47] Feng Gu, Shu Fen Wang, Meng Kai Lu, Guang Jun Zhao, Dong Xu, and Duo Ronq Yuan, J. Phys. Chem. B **108**, 8119 (2004).
[48] H. P. Plug and L. E. Alexander, *X-ray Diffraction Procedures for Polycrystalline and Amorphous Material* (Wiley, New York, 1954).
[49] O. Nagai, N. L. Bonavito, and T. Tanaka, J. Phys. C **6**, L470 (1973).
[50] B. D. Cullity, *Introduction to Magnetic Materials* (Addison-Wesley, Reading, MA, 1972).
[51] R. D. Zysler, D. Fiorani, A. M. Testa, L. Suber, E. Agostinelli, and M. Godinho, Phys. Rev. B **68**, 212408 (2003).
[52] N. Amin and S. Arajs, Phys. Rev. B **35**, 4810 (1987).
[53] Y. Y. Xu, X. F. Rui, Y. Fu, and H. Zhang, Chem. Phys. Lett. **410**, 36 (2005).
[54] R. D. Zysler, M. Vasquez–Mansilla, C. Arciprete, M. Dimitrijewits, D. Rodriguez–Sierra, and C. Saragovi, J. Magn. Magn. Mater. **224**, 39 (2001).
[55] R. D. Zysler, D. Fiorani, and A. M. Testa, J. Magn. Magn. Mater. **224**, 5 (2001).
[56] F. J. Berry, C. Greaves, O. Helgason, J. Mcmanus, H. M. Palmer, and R. T. Williams, J. Solid State Chem. **151**, 157 (2000).
[57] T. Ericsson, A. Krishnamurthy, and B. K. Srivastava, Phys. Scr. **33**, 88 (1986).
[58] H. Ting, L. He-Lie, and L. Shi, J. Magn. Magn. Mater. **71**, 323 (1988).
[59] R. E. Vandenberghe, A. H. Verbeeck, and E. De Grave, J. Magn. Magn. Mater. **54-57**, 898 (1986).
[60] David. J. Dunlop and Ozden Ozdemir, *Rock Magnetism: Fundamental and Frontiers* (Cambridge University Press, Cambridge, 1997), p. 69.